Supporting Information

Anode Overpotential Control via Interfacial Modification: Inhibition of Lithium Plating on Graphite Anodes

Killian R. Tallman[a], Bingjie Zhang[a], Lei Wang[b], Shan Yan[b], Katherine Thompson[c,d], Xiao Tong[e], Juergen Thieme[f], Andrew Kiss[f], Amy C. Marschilok[a, b, g], Kenneth J. Takeuchi[a, g], David C. Bock[b], Esther S. Takeuchi[a, b, g]**

[a] Department of Chemistry, Stony Brook University, Stony Brook, NY 11794, USA

[b] Energy Sciences Directorate, Brookhaven National Laboratory, Upton, NY 11973 USA

[c] Department of Chemistry and Physics, Mansfield University of Pennsylvania, Mansfield PA 16933 USA.

[d] Science Undergraduate Laboratory Internship (SULI) Program, Brookhaven National Laboratory, Upton, NY 11973 USA.

[e] Center for Functional Nanomaterials, Brookhaven National Laboratory, Upton, NY 11973 USA

[f] National Synchrotron Light Source II, Brookhaven National Laboratory, Upton, NY 11973 USA

[g] Department of Materials Science and Chemical Engineering, Stony Brook University, Stony Brook, NY 11794, USA

* corresponding authors: (DCB: dbock@bnl.gov, EST: esther.takeuchi@stonybrook.edu)

Graphite Characterization:

Scanning electron microscopy measurements were performed on the natural graphite powder. Figure S1 shows SEM images of the material, as well as the distribution of particle sizes determined from SEM imaging. Graphite powder particles have a flake like morphology with nanometer thin layers apparent on the surface. Graphite particle size diameters range between 4 – 11 µm, with average particle size of 7 ± 1 µm (n = 170). BET surface area is 1.86 ± 0.01 m^2/g. Synchrotron X-ray diffraction measurements were performed at NSLS-II beam line 28-ID to confirm the purity of the graphite. Structural refinements of the XRD patterns using the Rietveld method is shown in Figure S2. Refinement of the SLC1506T natural graphite indicated that the material was a mixture of both hexagonal (Space group $P6_3/mmc$ space group, 77%) and rhombohedral ($R\bar{3}m$ space group, 23%) phases and was free of impurities.

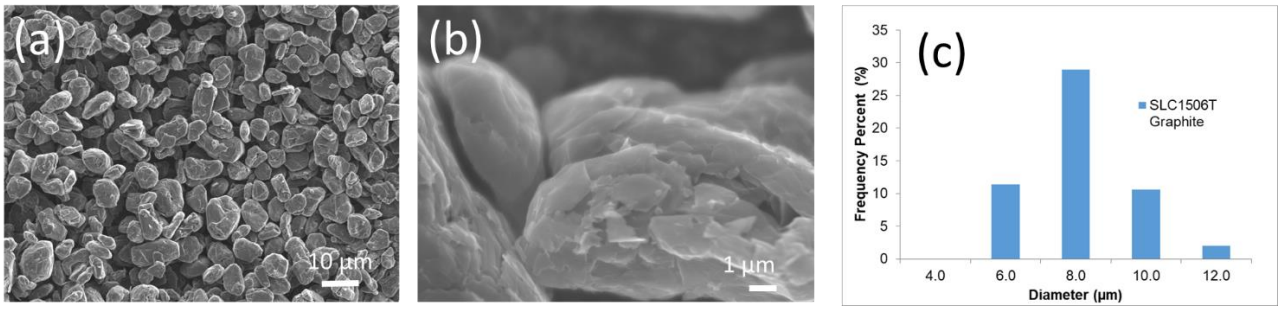

Figure S1. (a, b) Scanning electron microscopy characterization for the natural graphite used in this study. (c) Particle size distribution determined from SEM images.

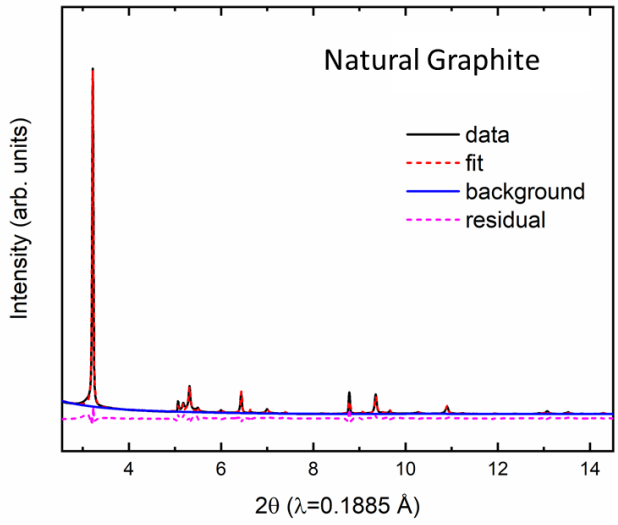

Figure S2. Rietveld refinement of synchrotron X-ray diffraction collected on the natural graphite.

Table S1. Calculated impact of 10 nm metal surface films on the irreversible capacity and cell specific energy for a theoretical 1 Ah NMC622/graphite pouch cell with total 320 cm^2 electrode area (anode), 10 mg/cm^2 anode loading, and negative to positive capacity ratio of 1.15 for the uncoated anode.

Anode Type	**Mass of metal films (mg/cell)**	**Additional Irreversible Capacity (mAh/cell)**	**% of Li inventory lost by metal oxide reduction**	**N:P ratio**	**Cell Specific Energy (Wh/kg)**
graphite	n/a	n/a	n/a	1.150	188.33
Cu-graphite	2.02	1.36	0.13%	1.152	188.06
Ni-graphite	2.13	1.53	0.15%	1.152	188.03

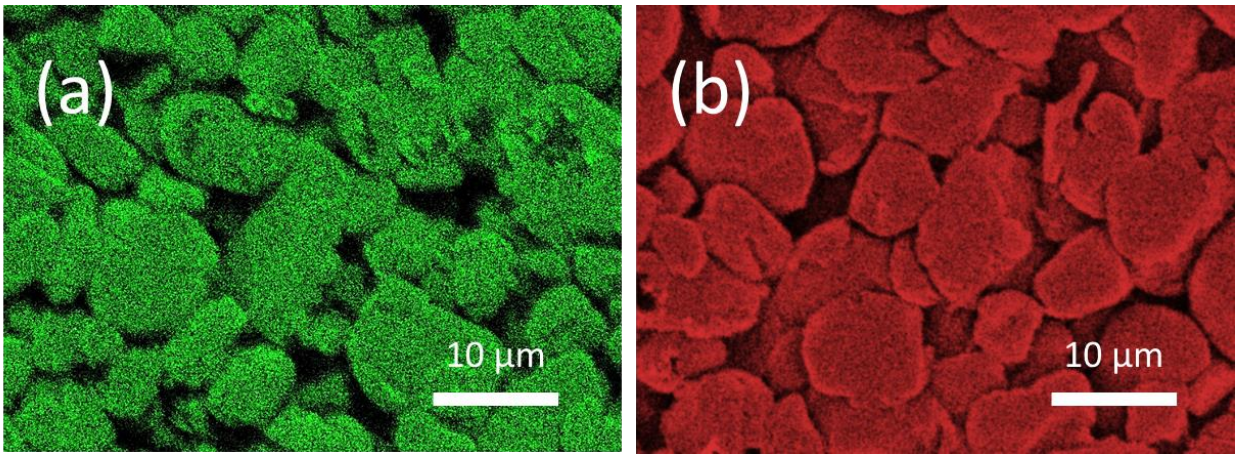

Figure S3. EDS maps collected from the top down for (a) 10 nm Cu-graphite and (b) 10 nm Ni-graphite.

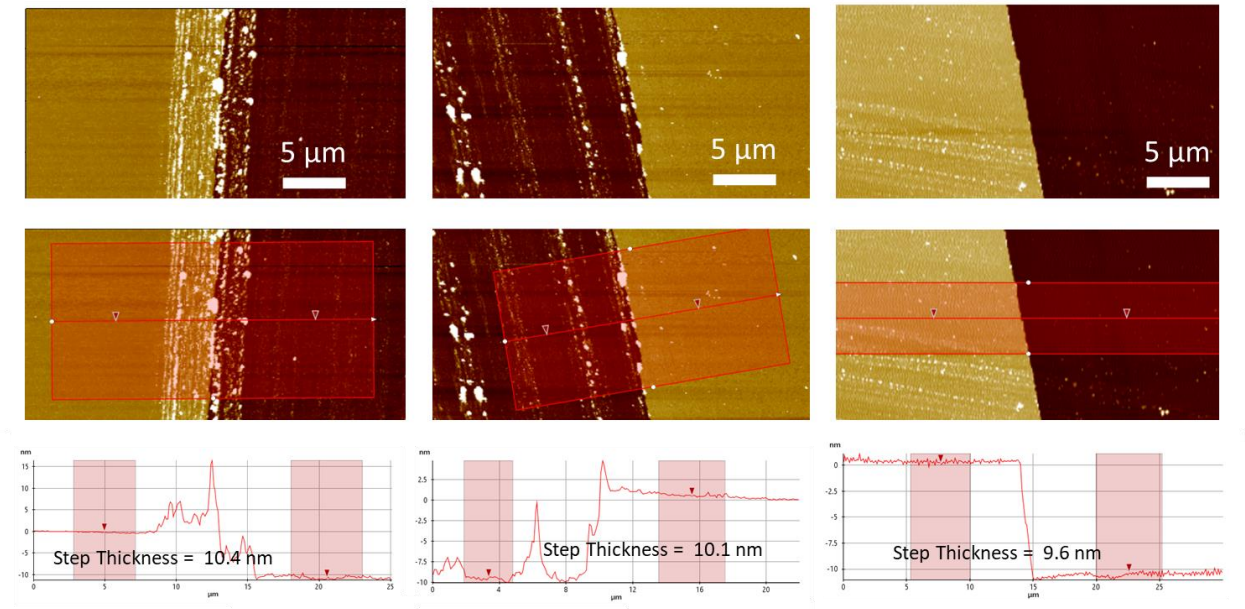

Figure S4. Representative atomic force microscopy images of ultra-flat SiO_2 wafers sputtered with 10 nm of Cu. Post-sputtering, a portion of the deposited coating was removed from the wafer by scratching with a pair of fine-tipped metal tweezers, creating a step between the metal coated and uncoated areas that was then analyzed by non-contact AFM. The process does not scratch the SiO_2 wafer itself; however, it can result in surface roughness in the crevice if the metal coating was not completely removed. Regions with minimized surface roughness were selected for AFM analysis. The middle and bottom panels in the figure show the stepped areas analyzed and the corresponding surface profile data.

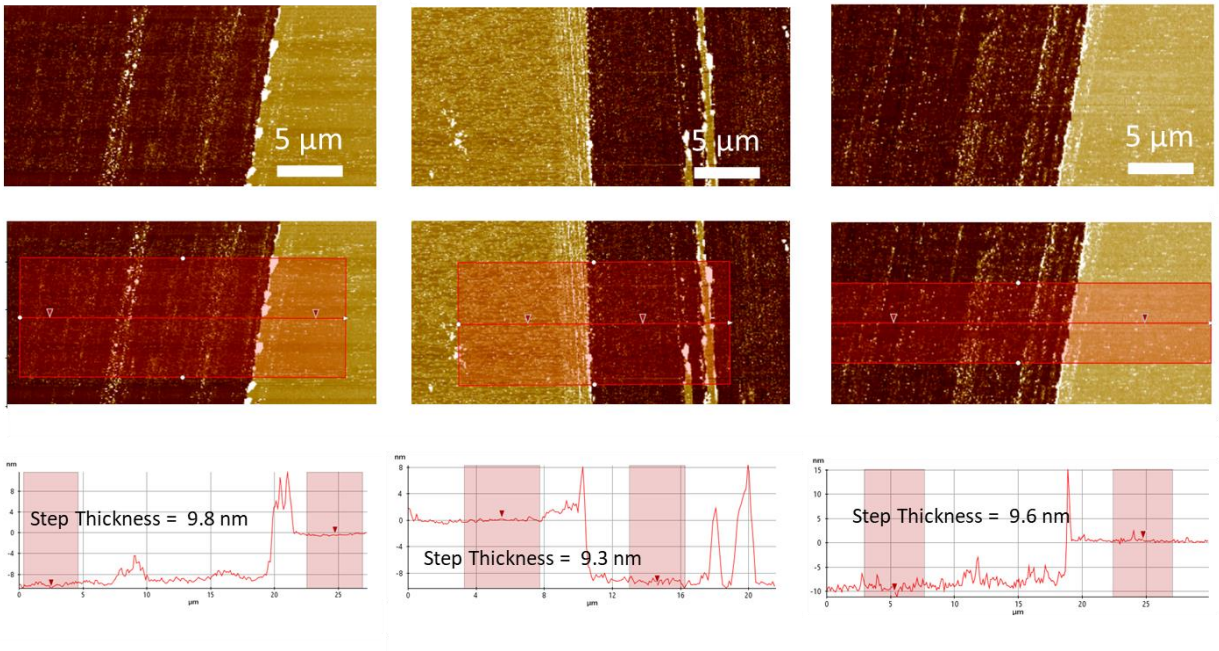

Figure S5. Representative atomic force microscopy images of ultra-flat SiO_2 wafers sputtered with 10 nm of Ni. Post-sputtering, a portion of the deposited coating was removed from the wafer by scratching with a pair of fine-tipped metal tweezers, creating a step between the metal coated and uncoated areas that was then analyzed by non-contact AFM. The process does not scratch the SiO_2 wafer itself; however, it can result in surface roughness in the crevice if the metal coating was not completely removed. Regions with minimized surface roughness were selected for AFM analysis. The middle and bottom panels in the figure show the stepped areas analyzed and the corresponding surface profile data.

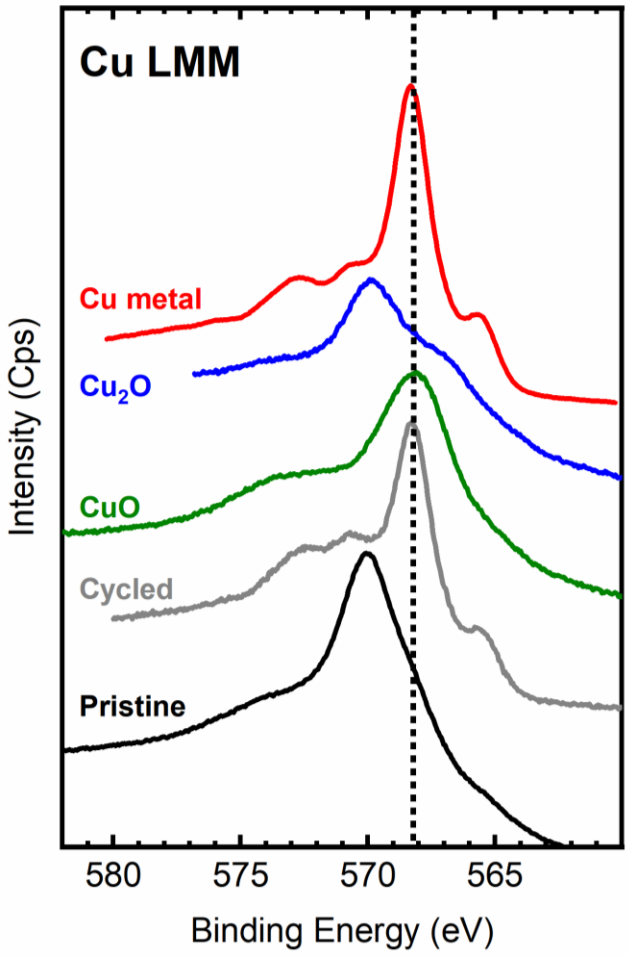

Figure S6. X-ray generated Auger LMM spectra for Cu standards compared to 10 nm Cu-graphite electrode in the pristine state as well as after formation cycling.

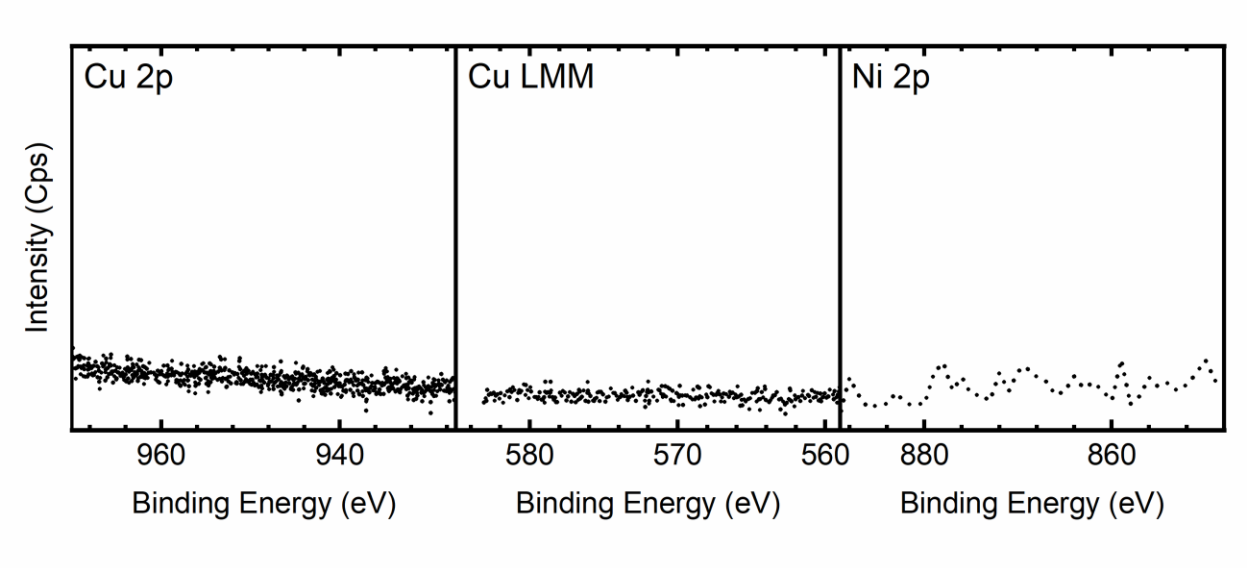

Figure S7. XPS Cu 2p, Cu LMM, and Ni 2p spectra collected on electrodes that underwent formation cycling. No signals were observed prior to Ar sputtering.

Table S2. Cu 2p and Ni 2p XPS peak assignments for Cu-graphite and Ni-graphite anodes before and after formation cycling.

Sample	As prepared		After formation cycling	
XPS Fit	B.E. (fwhm) Area	Assignment	B.E. (fwhm) Area	Assignment
Cu $2p_{3/2}$	943.8 (3.7) 1.4E4	CuO satellite		
	941.4 (4.6) 1.5E4	CuO satellite		
	933.6 (4.1) 7.6E4	CuO		
	932.6 (1.6) 5.3E4	$Cu_2O + Cu^0$	932.6 (2.1) 1.0E4	Cu^0
Ni $2p_{3/2}$	863.9 (2.8) 2.0E4	NiO satellite		
	861.2 (4.1) 1.6E5	NiO satellite		
	855.8 (3.8) 2.4E5	NiO		
	854.0 (2.7) 8.1E4	NiO		
	858.7 (3.4) 1.8E4	Ni^0 satellite	859.2 (4.9) 3.9E4	Ni^0 satellite
	856.3 (2.0) 1.3E4	Ni^0 satellite	855.9 (2.3) 8.6E3	Ni^0 satellite
	852.6 (1.7) 6.9E4	Ni^0	852.6 (1.7) 2.2E5	Ni^0

Table S3. C 1s, O 1s, F 1s, and Li 1s XPS peak assignments for uncoated graphite (control), Cu-graphite, or Ni-graphite anodes after formation cycling.

Sample	Uncoated Anode	Cu Coated Anode	Ni Coated Anode	Assignment	
XPS Fit	B.E. (fwhm) area (rel. %)	B.E. (fwhm) area (rel. %)	B.E. (fwhm) area (rel. %)	Bond	Species
C 1s	290.1 (1.99) 1.2E4 (16)	289.9 (2.04) 1.2E4 (20)	289.9 (1.93) 1.5E4 (27)	CO_3	Carbonates (Li_2CO_3, $ROCO_2Li$)
	288.8 (2.22) 7.7E3 (10)	288.5 (2.00) 6.2E3 (10)	288.6 (1.83) 5.8E3 (11)	O–C=O	Carboxylates (RCOOLi, RCOOR')
	286.6 (2.05) 1.6E4 (22)	286.8 (1.63) 9.8E3 (17)	286.8 (1.89) 1.3E4 (23)	C–O	Ethers, PEO
	285.0 (2.01) 3.1E4 (42)	285.0 (1.92) 3.1E4 (53)	285.0 (1.91) 2.2E4 (39)	C–C/C–H	Hydrocarbons
	283.0 (1.36) 6.7E3 (9)			C–Li	Lithiated graphite
O 1s	533.7 (2.27) 3.8E4 (23)	533.7 (2.29) 3.5E4 (22)	533.7 (2.15) 3.5E4 (17)	C−O	PEO, Li alkyl carbonates
	531.8 (2.15) 1.3E5 (77)	531.8 (2.12) 1.3E5 (78)	531.8 (2.10) 1.7E5 (83)	C=O, C−O−C	Carbonates, carboxylates, ethers
F 1s	687.8 (2.45) 4.0E4 (50)			C−F	PVDF
	687.3 (2.49) 1.3E4 (17)	687.3 (2.65) 2.7E4 (33)	687.3 (2.37) 3.3E4 (42)	P−F	LiP_xF_y
	685.0 (1.91) 2.6E4 (33)	685.0 (1.99) 5.4E4 (67)	685.0 (1.93) 4.6E4 (58)	Li–F	LiF
Li 1s	55.3 (1.99) 1.7E3 (100)	55.4 (1.96) 2.2E3 (100)	55.4 (2.02) 2.5E3 (100)	Li–F, Li–O	LiF, Li_2CO_3, Li_2O

Surface composition of the SEI and electrode components for uncoated graphite, Cu-graphite and Ni-graphite electrodes after formation cycling were investigated using XPS in the regions of C 1s, O 1s, F 1s and Li 1s. The C 1s spectral fitting resulted in five distinct peaks (**Table S3**). Four peaks were observed for all three samples (uncoated graphite anode, Cu–coated anode, and Ni–coated anode) in the C 1s spectra.

The relative peak intensities for these four peaks are similar for each sample, indicating similar surface chemistry in the presence of the metal coatings. The highest binding energy peak at ~290.0 eV is attributed to carbonates which are commonly observed in similar systems.[1] Typically, SEI carbonate components formed on graphite anodes in the presence of alkyl carbonate solvents, such as EC and DMC, include Li_2CO_3[1] as well as a range of lithium alkyl carbonates, with the general form of $ROCO_2Li$.[1-7] It is likely that there is a combination of these types of carbonates present in the SEI layer, as it is difficult to deconvolute these chemically similar compounds. However, EC can undergo a one-electron reduction and a two-electron reduction to form $CH_3CH_2OCO_2Li$ and $(CH_2OCO_2Li)_2$, respectively, while DMC can undergo a one-electron reduction and a two-electron reduction to form CH_3OCO_2Li and Li_2CO_3, repectively.[1, 8] The C 1s peak at ~288.6 eV corresponds to carbon atoms in a two-oxygen environment. Such species that exist around this binding energy include esters and carboxylate-containing compounds.[9-10] With this electrolyte composition, it is likely that RCOOLi and RCOOR' moieties are present in the SEI at this binding energy.[11-12] The next C 1s peak at ~286.7 eV is assigned to C–O bonds and correspond to ether and alkoxy species.[5-6, 13] A commonly characterized oxygen-containing polymeric SEI species, typically denoted as polyethylene oxide (PEO, $[–CH_2–CH_2–O–]_n$), can be attributed here as it can often form as a reduction product of EC and DMC solvents.[1, 4, 14 1, 4, 14] There is an additional peak that exists for the uncoated graphite anode at 283.0 eV. This peak is commonly observed in SEI studies of graphite and is attributed in the literature to either lithiated

graphite species Li_xC_6[40, 48] or lithium carbide.[47, 49-50] As discussed in the manuscript, the Li–C peak is detected for the control graphite electrode but not for the metal coated electrodes because photoelectrons from lithiated graphite are inhibited by the thickness of the metal films and the SEI.

The O 1s spectra has two peaks, at ~533.7 and ~531.8 eV (**Figure 4**) and can be identified as C–O and C=O bonds, respectively. These bonds exist in most of the identified SEI species in the C 1s spectra, but most notably PEO, Li alkyl carbonates and other carbonate species.[1, 4, 6-7, 13] Each F 1s spectra has two peaks at ~687.3 and ~685.0 eV corresponding to P–F and Li–F bonds while only the uncoated spectra displays an additional peak at ~687.8 eV which correlates well with C–F peaks also found in the pristine spectra (**Figure S8**). Lastly, the Li 1s spectral region contains a broad peak at ~55.4 eV and is in the region of Li–F and Li–O bonding in the form of LiF, Li_2O and Li_2CO_3.[1, 3, 14, 17] Further spectral discussions are located in the main text, including analyses of the F 1s spectra.

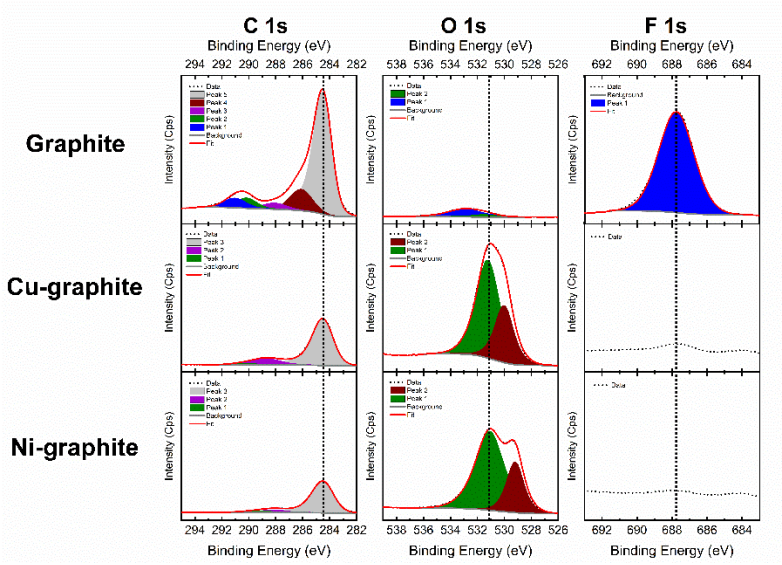

Figure S8. XPS C 1s, O 1s, and F 1s spectra for the as prepared uncoated graphite (control), Cu-graphite, or Ni-graphite anodes. Plots of each respective spectral region are on the same scale.

Table S4. C 1s, O 1s, and F 1s XPS peak assignments for the as prepared uncoated graphite (control), Cu-graphite, or Ni-graphite anodes.

Sample	Uncoated Anode	Cu Coated Anode	Ni Coated Anode	Assignment	
XPS Fit	B.E. (fwhm) area (rel. %)	B.E. (fwhm) area (rel. %)	B.E. (fwhm) area (rel. %)	Bond	Species
C 1s	291.0 (1.92) 1.4E4 (6)			C–F	PVDF
	290.2 (1.74) 1.4E4 (6)	290.4 (2.14) 1.9E3 (2)	289.5 (2.39) 2.7E3 (4)	CO_3	Carbonate (adsorbed)
	288.1 (2.02) 9.4E3 (13)	288.7 (2.48) 1.2E4 (13)	288.2 (1.95) 3.7E3 (6)	O–C=O	Adsorbed CO_x
	286.1 (1.89) 3.2E4 (13)			C–O	Adsorbed CO_x
	284.4 (1.56) 1.7E5 (72)	284.4 (1.80) 7.8E4 (85)	284.4 (1.88) 5.5E4 (90)	C–C sp2	Graphite
O 1s	533.0 (2.98) 1.5E4 (84)			C–O	Adsorbed CO_x
	531.5 (1.93) 2.8E2 (16)	531.2 (2.05) 1.3E5 (69)	531.0 (2.51) 1.3E5 (72)	C=O, C–O–C	Adsorbed CO_x
		530.0 (1.62) 5.9E4 (31)		Ni–O	NiO
			529.1 (1.50) 4.9E4 (28)	Cu–O	CuO
F 1s	687.8 (2.36) 2.2E5 (100)	687.7 (1.94) 1.7E4 (100)	687.8 (1.97) 6.3E3 (100)	C–F	PVDF

Surface composition of the as prepared electrode surface for uncoated graphite, Cu-graphite and Ni-graphite electrodes were investigated using XPS in the regions of C 1s, O 1s, and F 1s. Fitting results are displayed in **Figure S8** and reported in **Table S4**. The C 1s spectra for each electrode reveals graphitic carbon as the dominate contributor to the signal. Additionally, there are various carbon-oxygen bonds present that relate to an array of adventitious carbon (CO_x) adsorbed on the surface.[18] The metal coated electrodes match well with each other as similar peak profiles are exhibited. As expected based on the inelastic mean free path of C 1s photoelectrons, the graphitic peak at 284.4 eV is significantly dampened by the presence of the 10 nm Cu or Ni metal films. The graphitic peak is reduced on average by a factor of ~5 which is due to a ~9 nm sampling depth.[7, 19-20] Another noteworthy difference between the uncoated and metal coated electrodes is the presence of F-containing species. There is a clear C–F peak at ~291.0 eV, corresponding to the PVDF binder, in the uncoated C 1s spectra but is absent in both metal coated spectra. Moreover, this difference is displayed in the F 1s spectra as well. The uncoated graphite has a PDVF peak at ~687.8 eV while the metal coated F 1s spectra have a peak hardly distinguishable from the background at the same binding energy. The peak areas show that the PVDF peak for the uncoated graphite is more intense then the metal coated PVDF peaks on average by a factor of ~20. This stronger dampening effect of the F 1s signal relative to the C 1s signal is because of its lower kinetic energy, which has a sampling depth of ~7 nm.[7, 21]

The O 1s spectra are all quite different between the three electrodes. The uncoated graphite surface has two peaks that align well with bonds found in adsorbed CO_x species.[11] One single peak relating to CO_x species or possibly defective oxide species exists at ~531.1 eV for both metal coated electrodes.[11, 22-23] However, for Cu-graphite surface there is a second peak at ~530.0 eV which agrees well with a lattice oxide in a Cu_2O phase.[22] Similarly, the second Ni-graphite at ~529.1 eV matches well with lattice oxide in a NiO phase.[23] The O 1s spectra identifies absorbed

CO_x species on the surface of uncoated graphite while it also confirms the presence of an oxidized metal surface in both metal coated electrodes corroborating results from the Cu 2p/LMM and Ni 2p transitions.

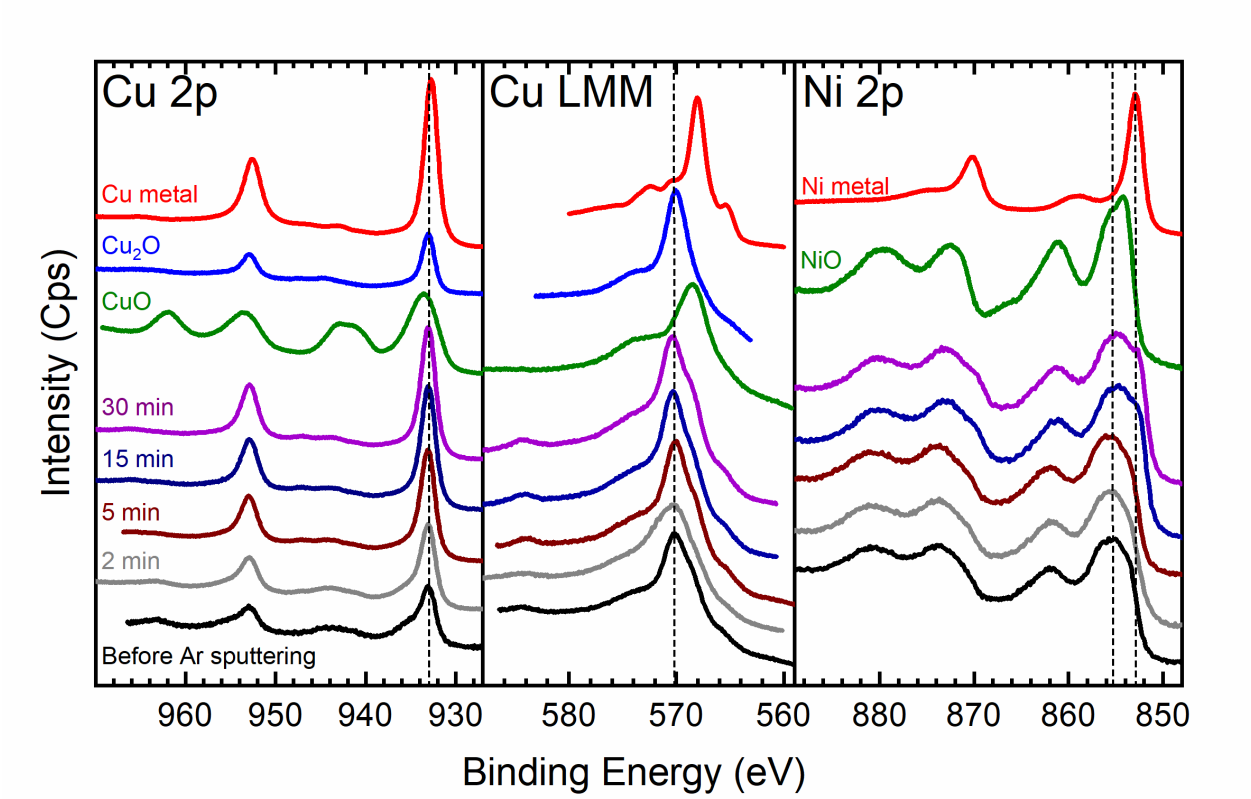

Figure S9. XPS Cu 2p, Cu LMM, and Ni 2p spectra for the as prepared Cu-graphite and Ni-graphite anodes as a function of Ar sputtering times: 0, 2, 5, 15, 30 minutes. Cu metal, Cu_2O, CuO, Ni metal and NiO are plotted for comparison. The dominant species are Cu and Ni oxides before and after Ar sputtering.

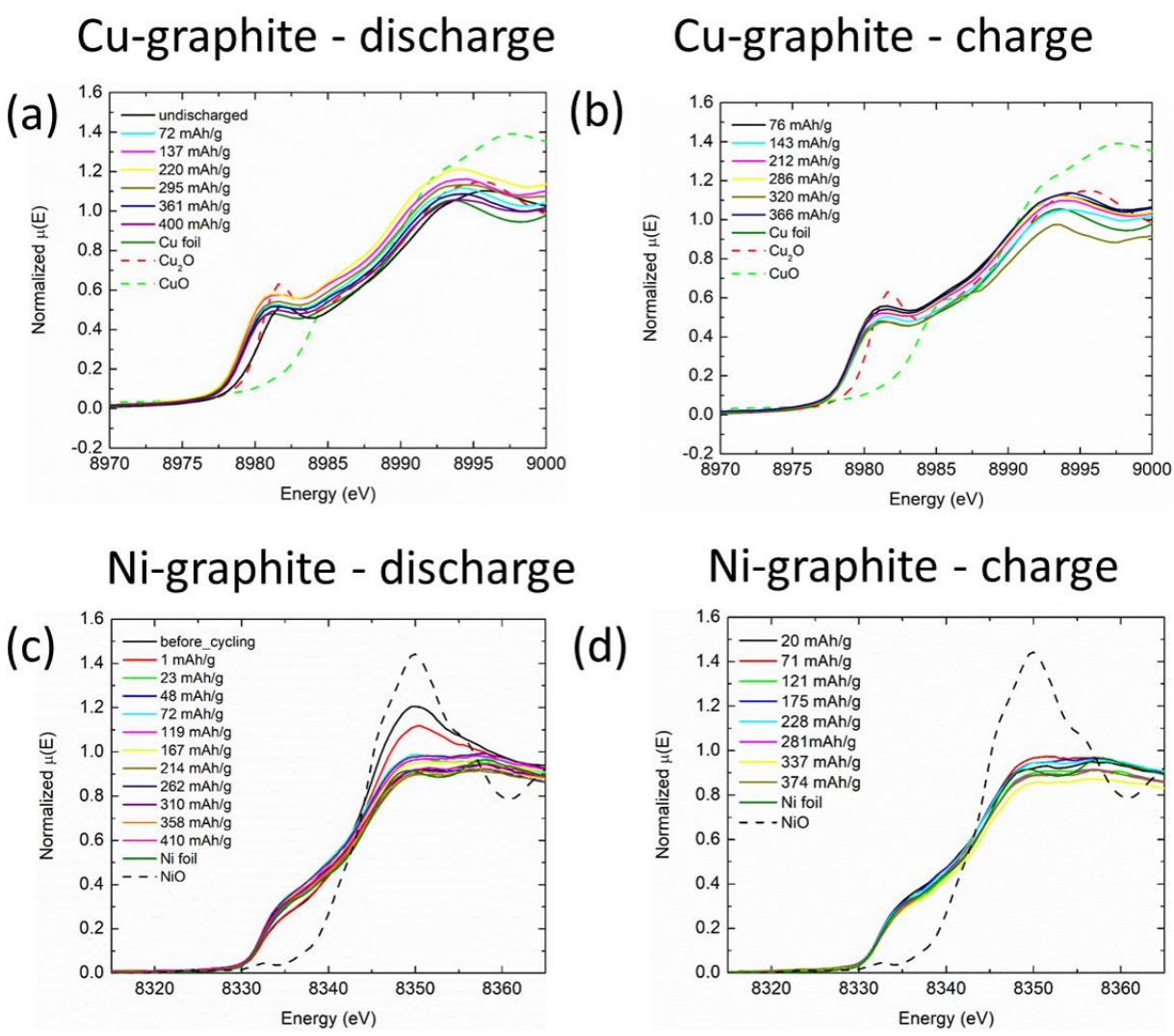

Figure S10. *Operando* XANES spectra overlaid with relevant standards for (a, b) Cu-graphite electrodes and (c, d) Ni-graphite electrodes during a single formation cycle at C/5 rate between 0.01–1.3 V vs. Li/Li^+. Spectra are shown for (a, c) discharge and (b, d) charge processes.

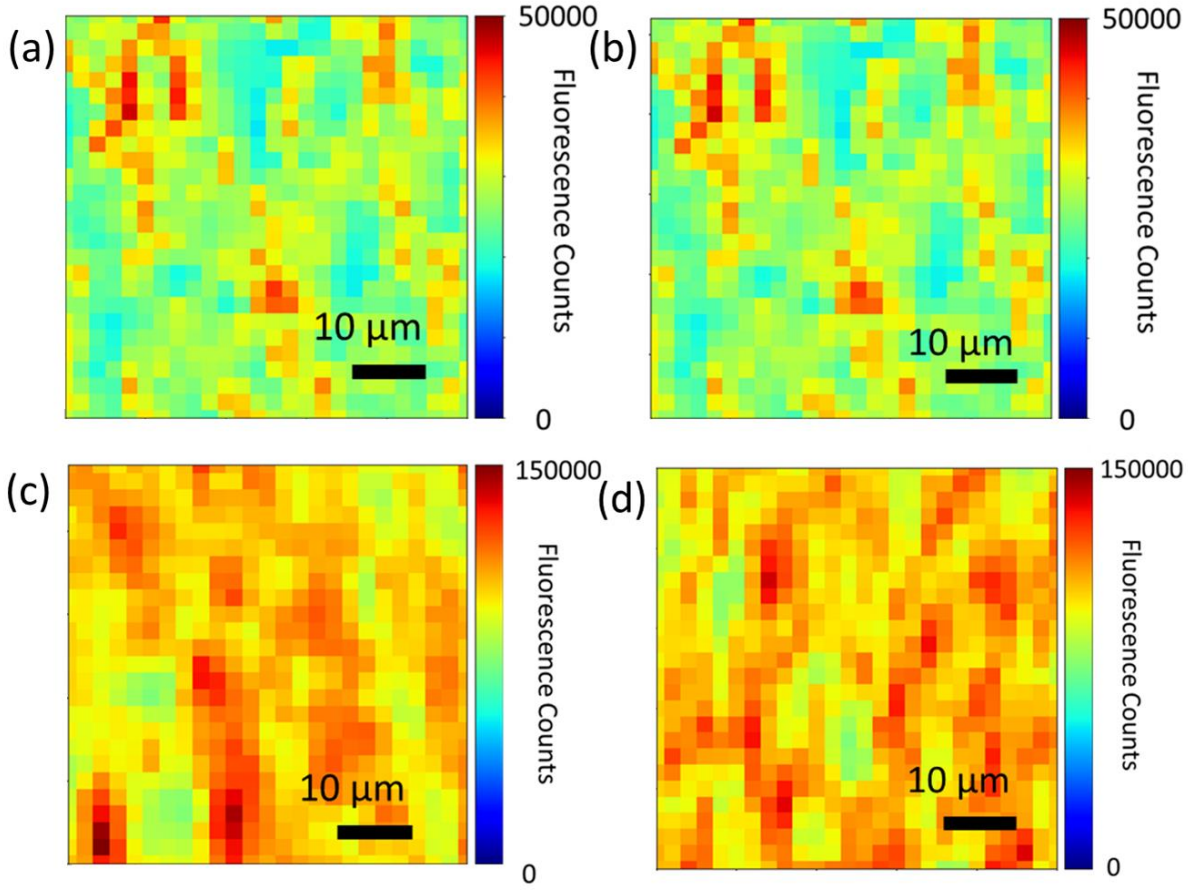

Figure S11. (a, b, c, d) XRF maps of (a) pristine 10 nm Cu-graphite electrode, (b) 10 nm Cu-graphite electrode after formation cycling (c) pristine 10 nm Ni-graphite electrode (d) 10 nm Ni-graphite electrode after formation cycling.

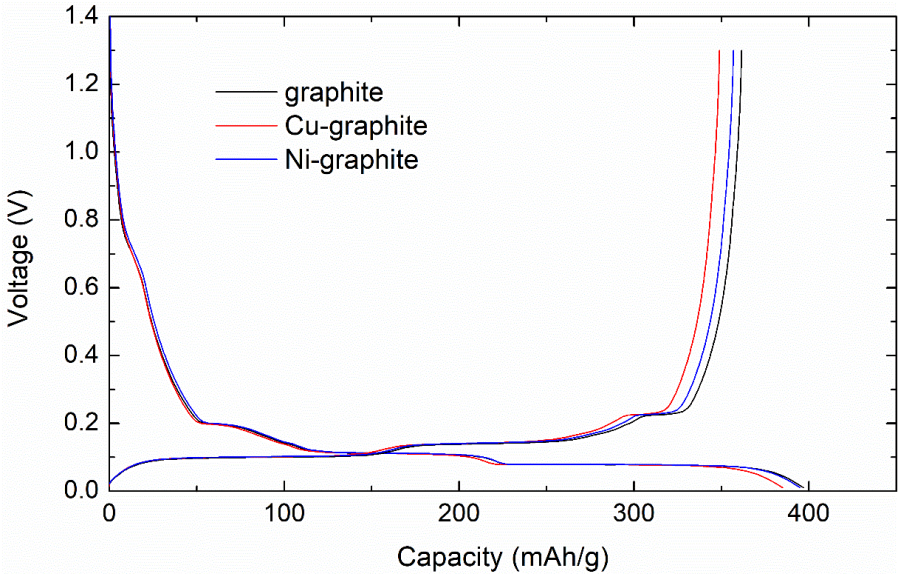

Figure S12. First discharge and charge curves of graphite, 10 nm Cu-graphite, 10 nm Ni-graphite electrodes at C/10 rate between 0.01–1.3 V.

Table S5. Tabulated capacity values for first discharge and charge of electrodes at C/10 rate between 0.01–1.3 V (n = 4).

Electrode	1st lithiation $mAhg^{-1}$	1st delithiation $mAhg^{-1}$	Irreversible Capacity $mAhg^{-1}$
graphite	399 ± 5	362 ± 5	37 ± 7
Cu-graphite	388 ± 5	353 ± 5	35 ± 8
Ni-graphite	394 ± 4	356 ± 5	38 ± 6

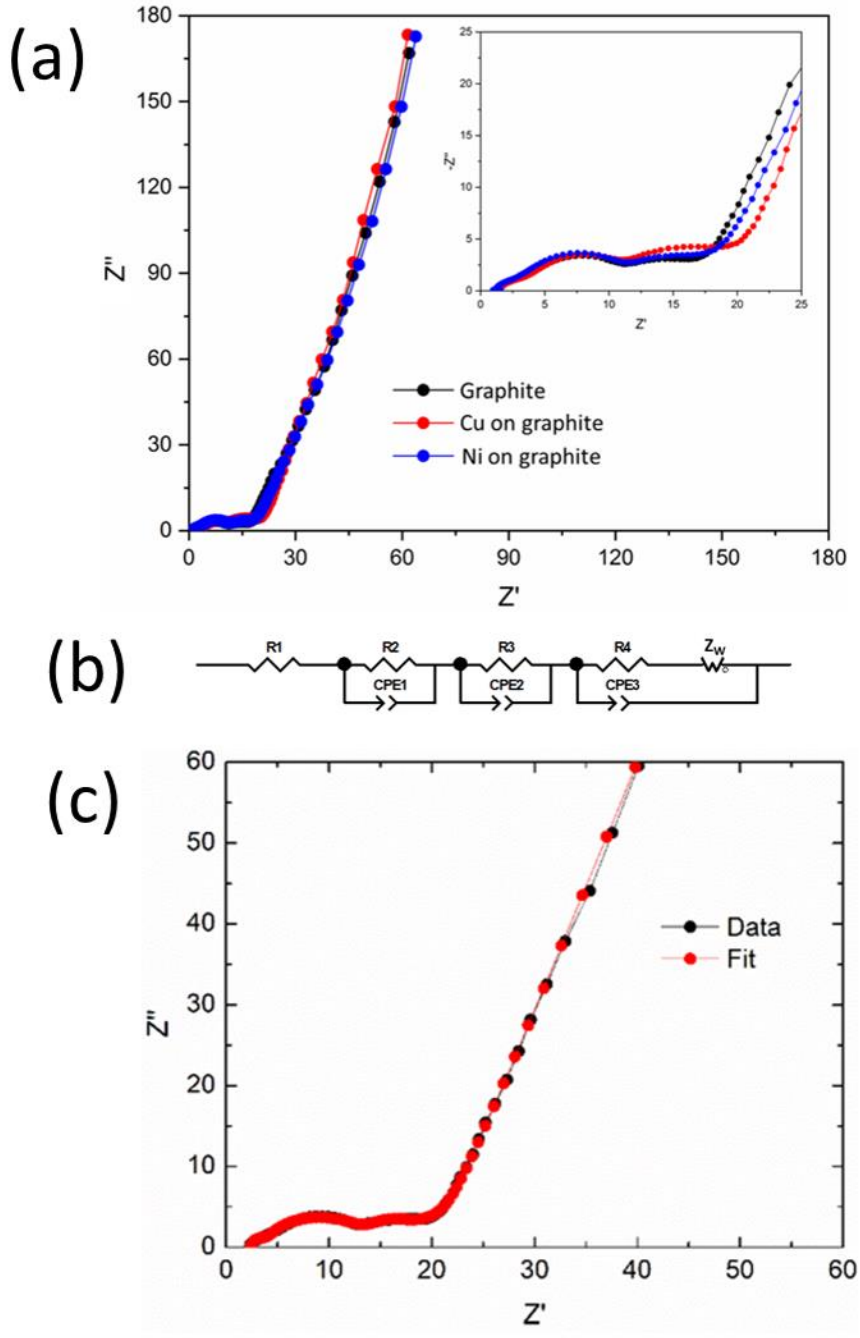

Figure S13. (a) Comparison of representative EIS spectra after formation cycling for pristine graphite electrodes, graphite electrodes sputtered with 10 nm Cu, and graphite electrodes sputtered with 10 nm of Ni. (b) Equivalent circuit model used to quantify the impedance data. (c) Example overlay of experimental data and fit using the model.

Table S6. Tabulated average EIS equivalent circuit fit results (n = 4) for half cells after undergoing formation cycling.

Electrode Type	R_1 (Ω)	R_2 (Ω)	R_3 (Ω)	R_4 (Ω)	$Z_{w,R}$ (Ω)	$Z_{w,T}$ (Ω)	$Z_{w,P}$
graphite	1.5 ± 0.3	1.9 ± 0.3	8.1 ± 0.5	1.5 ± 0.3	15 ± 1	0.73 ± 0.07	0.399 ± 0.002
Cu-graphite	1.5 ± 0.5	2.6 ± 0.4	8.5 ± 0.7	1.5 ± 0.1	18 ± 2	0.9 ± 0.1	0.402 ± 0.003
Ni-graphite	1.7 ± 0.5	1.9 ± 0.1	7.8 ± 0.8	1.2 ± 0.2	16 ± 2	0.77 ± 0.06	0.403 ± 0.004

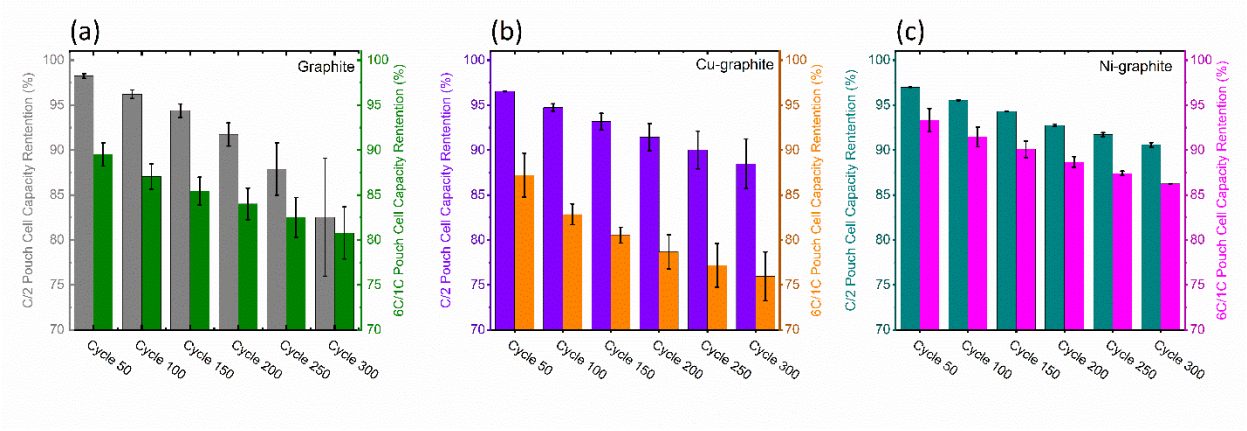

Figure S14. Columbic efficiency comparisons between C/2 and 6C/1C cycling of full pouch cells to assess fade rate. Each cell efficiency values are shown as an average and standard deviation of n = 2.

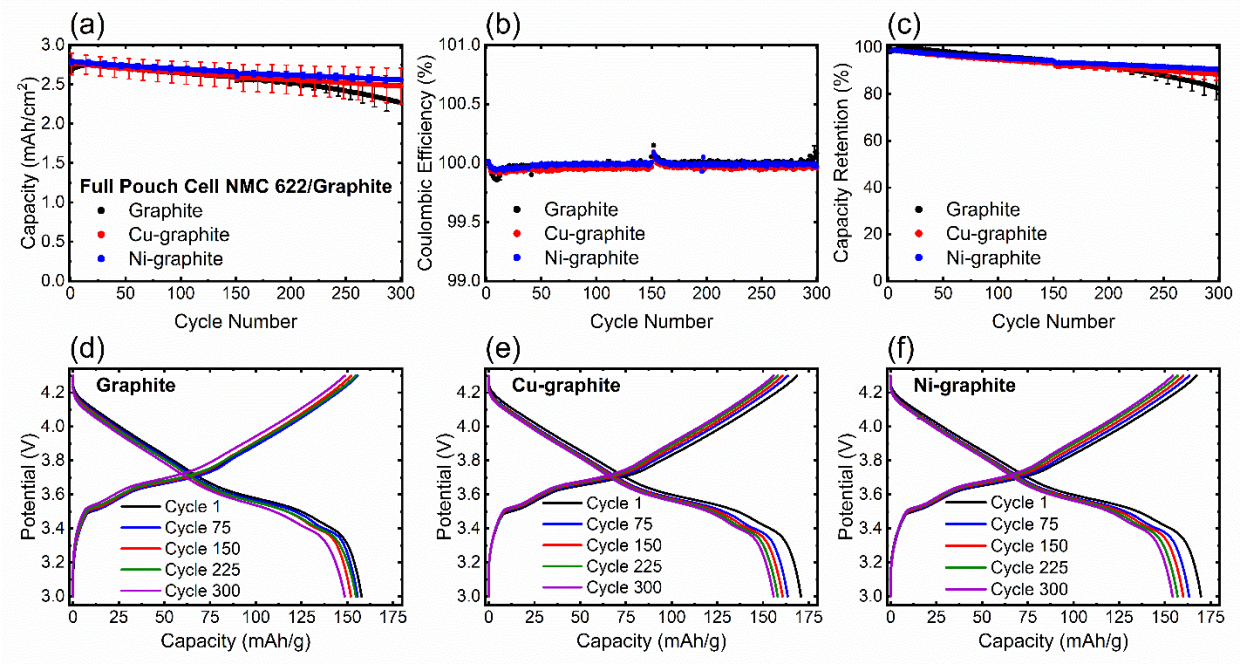

Figure S15. Electrochemistry of graphite/NMC622 cells under symmetric C/2 discharge and charge conditions. (a) areal capacities, and (b) coulombic efficiency, and (c) capacity retention. Representative voltage profiles for (d) graphite, (e) Cu-graphite, and (f) Ni-graphite. Anodes in the cells consisted of pristine graphite electrodes, graphite electrodes sputtered with 10 nm Cu, or graphite electrodes sputtered with 10 nm of Ni. Error bars represent one standard deviation from the mean (n = 2).

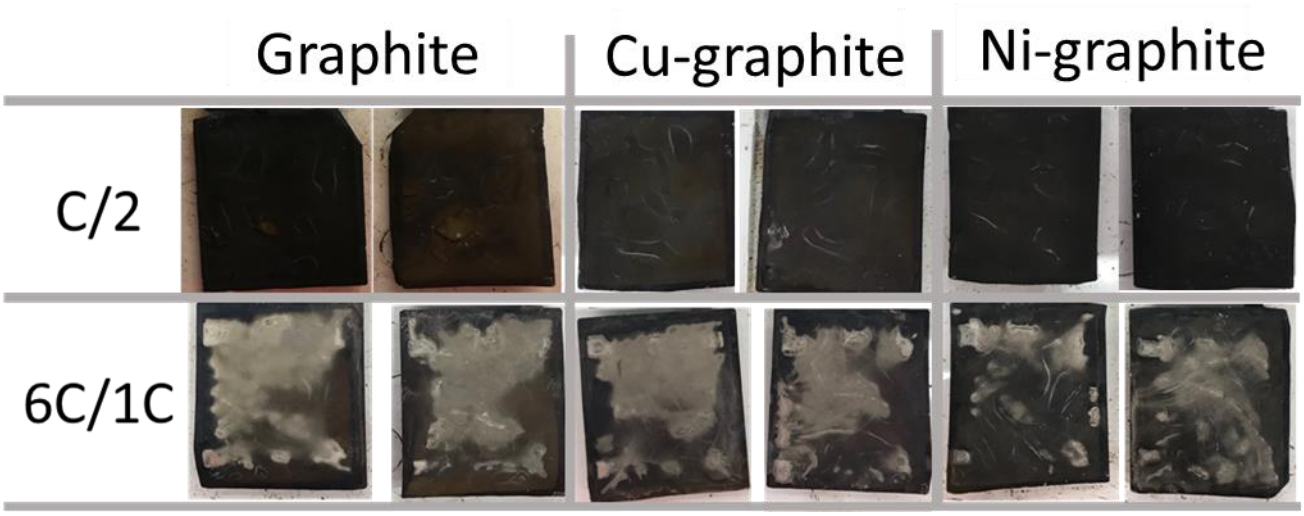

Figure S16. Images of anodes post 300 cycles at C/2 and 6C/1C rates in NMC622/graphite full pouch cells. Cells were in the charged state upon disassembly. The white-grey colored regions, apparent for the cells cycled at the 6C rate, is deposited Li metal.

Table S7. Normalized lithium plating capacities for fully lithiated electrodes subjected to voltage holds of -10, -15 and -20 mV for 6 hours.

Electrode Type	Normalized Li Plating Capacities		
	-10 mV voltage hold	-15 mV voltage hold	-20 mV voltage hold
graphite	0.30 ± 0.03	0.65 ± 0.05	1.00 ± 0.05
Cu-graphite	0.20 ± 0.05	0.48 ± 0.05	0.65 ± 0.03
Ni-graphite	0.20± 0.08	0.48 ± 0.03	0.60 ± 0.03

Table S8. Normalized Li(110)/Cu(220) peak area ratios from XRD measurements of electrodes recovered from half cells subjected to voltage holds of -10, -15 and -20 mV for 6 hours.

Electrode Type	Normalized Li(110)/Cu(220) Peak Area Ratio		
	-10 mV voltage hold	-15 mV voltage hold	-20 mV voltage hold
graphite	0.26 ± 0.03	0.49 ± 0.09	1.00 ± 0.08
Cu-graphite	0.13 ± 0.05	0.28 ± 0.08	0.6 ± 0.1
Ni-graphite	0.08 ± 0.08	0.28 ± 0.08	0.54 ± 0.05

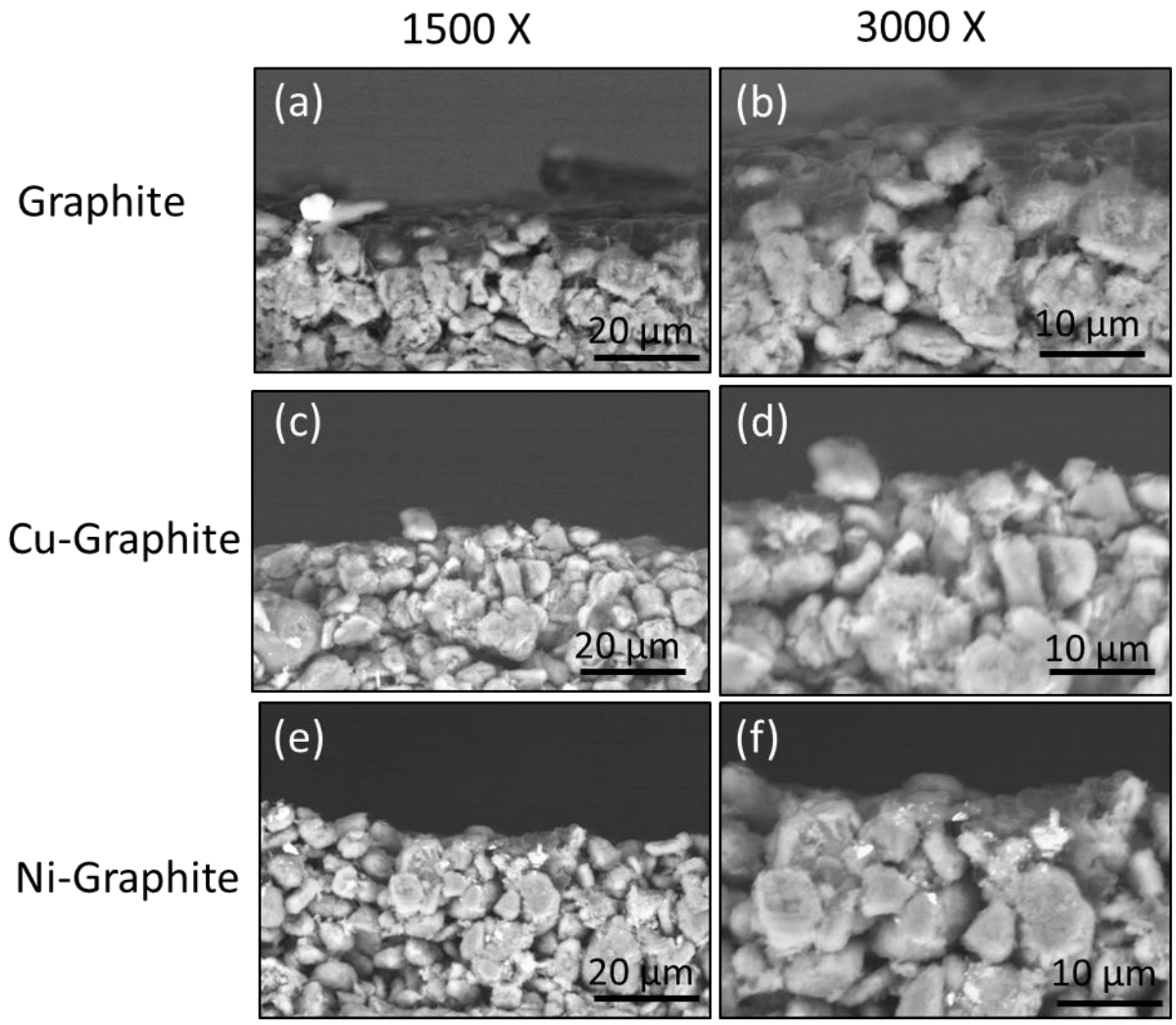

Figure S17. Cross-section SEM images at different magnifications of the Li plated on the (a-c) uncoated graphite, (d-f) Cu-coated graphite, and (g-i) Ni-coated graphite electrodes at 5000x magnification.

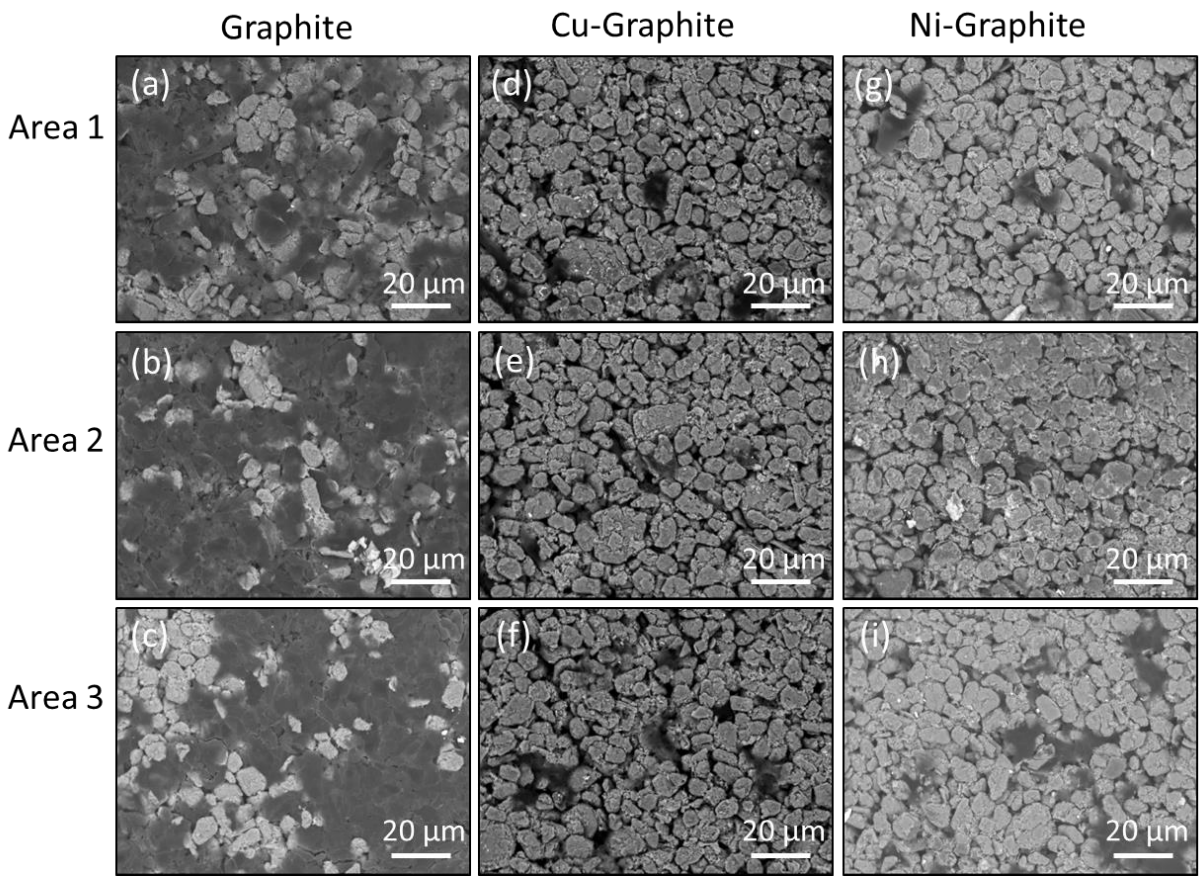

Figure S18. Backscatter SEM images at different magnifications of the Li plated on the (a-c) uncoated graphite, (d-f) Cu-coated graphite, and (g-i) Ni-coated graphite electrodes at 1000x magnification.

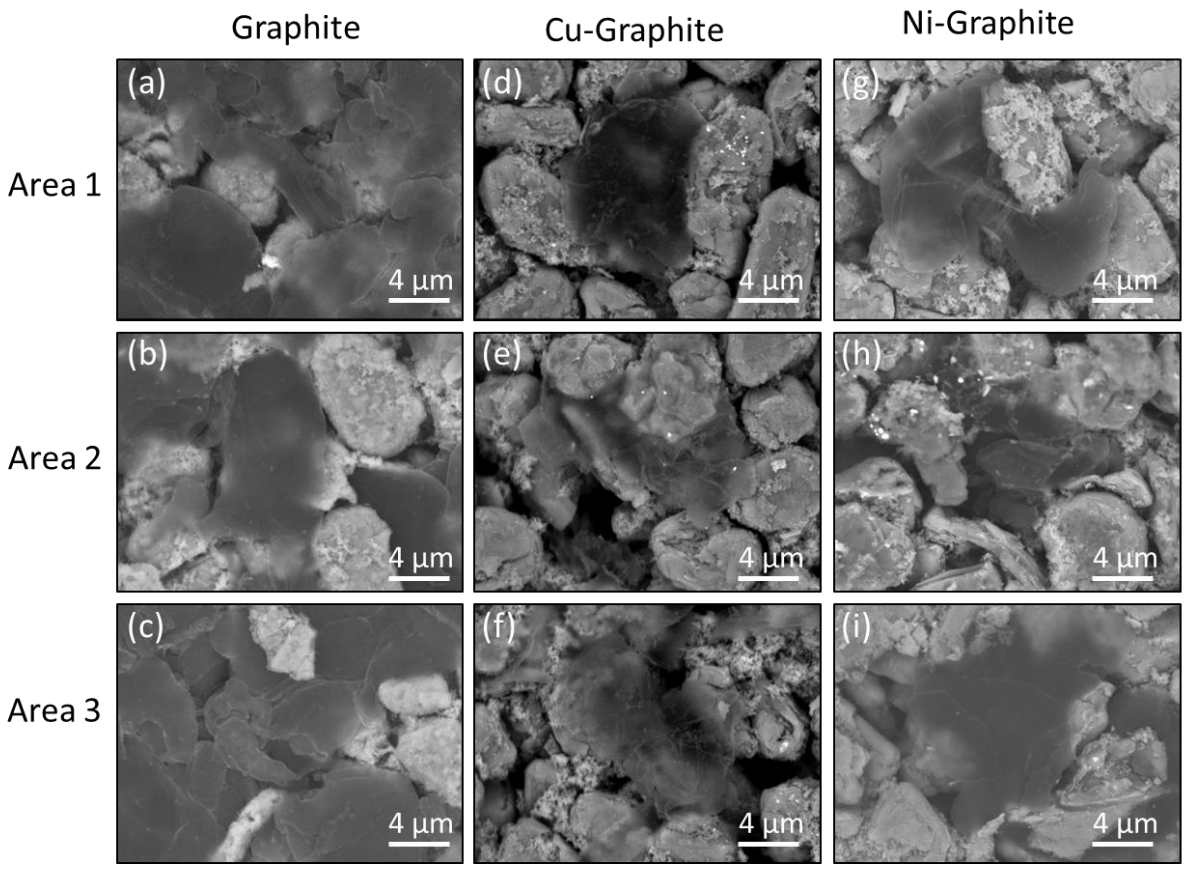

Figure S19. Backscatter SEM images at different magnifications of the Li plated on the (a-c) uncoated graphite, (d-f) Cu-coated graphite, and (g-i) Ni-coated graphite electrodes at 5000x magnification.

References

1. Verma, P.; Maire, P.; Novák, P., A review of the features and analyses of the solid electrolyte interphase in Li-ion batteries. *Electrochimica Acta* **2010,** *55* (22), 6332-6341.
2. Aurbach, D.; Markovsky, B.; Weissman, I.; Levi, E.; Ein-Eli, Y., On the correlation between surface chemistry and performance of graphite negative electrodes for Li ion batteries. *Electrochimica Acta* **1999,** *45* (1), 67-86.
3. Leroy, S.; Blanchard, F.; Dedryvère, R.; Martinez, H.; Carré, B.; Lemordant, D.; Gonbeau, D., Surface film formation on a graphite electrode in Li-ion batteries: AFM and XPS study. *Surface and Interface Analysis* **2005,** *37* (10), 773-781.
4. Andersson, A. M.; Henningson, A.; Siegbahn, H.; Jansson, U.; Edström, K., Electrochemically lithiated graphite characterised by photoelectron spectroscopy. *Journal of Power Sources* **2003,** *119-121*, 522-527.
5. Zhao, L. W.; Watanabe, I.; Doi, T.; Okada, S.; Yamaki, J., TG-MS analysis of solid electrolyte interphase (SEI) on graphite negative-electrode in lithium-ion batteries. *Journal of Power Sources* **2006,** *161* (2), 1275-1280.
6. Bryngelsson, H.; Stjerndahl, M.; Gustafsson, T.; Edström, K., How dynamic is the SEI? *Journal of Power Sources* **2007,** *174* (2), 970-975.
7. Malmgren, S.; Ciosek, K.; Hahlin, M.; Gustafsson, T.; Gorgoi, M.; Rensmo, H.; Edström, K., Comparing anode and cathode electrode/electrolyte interface composition and morphology using soft and hard X-ray photoelectron spectroscopy. *Electrochimica Acta* **2013,** *97*, 23-32.
8. An, S. J.; Li, J.; Daniel, C.; Mohanty, D.; Nagpure, S.; Wood, D. L., The state of understanding of the lithium-ion-battery graphite solid electrolyte interphase (SEI) and its relationship to formation cycling. *Carbon* **2016,** *105*, 52-76.
9. Schulz, N.; Hausbrand, R.; Dimesso, L.; Jaegermann, W., XPS-Surface Analysis of SEI Layers on Li-Ion Cathodes: Part I. Investigation of Initial Surface Chemistry. *Journal of The Electrochemical Society* **2018,** *165* (5), A819-A832.
10. Leroy, S.; Martinez, H.; Dedryvère, R.; Lemordant, D.; Gonbeau, D., Influence of the lithium salt nature over the surface film formation on a graphite electrode in Li-ion batteries: An XPS study. *Applied Surface Science* **2007,** *253* (11), 4895-4905.
11. Pantea, D.; Darmstadt, H.; Kaliaguine, S.; Roy, C., Electrical conductivity of conductive carbon blacks: influence of surface chemistry and topology. *Applied Surface Science* **2003,** *217* (1), 181-193.
12. Lu, W.; Xiong, S.; Xie, K.; Pan, Y.; Zheng, C., Identification of solid electrolyte interphase formed on graphite electrode cycled in trifluoroethyl aliphatic carboxylate-based electrolytes for low-temperature lithium-ion batteries. *Ionics* **2016,** *22* (11), 2095-2102.
13. Bock, D. C.; Waller, G. H.; Mansour, A. N.; Marschilok, A. C.; Takeuchi, K. J.; Takeuchi, E. S., Investigation of Solid Electrolyte Interphase Layer Formation and Electrochemical Reversibility of Magnetite, Fe3O4, Electrodes: A Combined X-ray Absorption Spectroscopy and X-ray Photoelectron Spectroscopy Study. *The Journal of Physical Chemistry C* **2018,** *122* (26), 14257-14271.
14. Niehoff, P.; Passerini, S.; Winter, M., Interface Investigations of a Commercial Lithium Ion Battery Graphite Anode Material by Sputter Depth Profile X-ray Photoelectron Spectroscopy. *Langmuir* **2013,** *29* (19), 5806-5816.
15. Ellis, L. D.; Allen, J. P.; Hill, I. G.; Dahn, J. R., High-Precision Coulometry Studies of the Impact of Temperature and Time on SEI Formation in Li-Ion Cells. *Journal of The Electrochemical Society* **2018,** *165* (7), A1529-A1536.

16. Ota, H.; Sakata, Y.; Inoue, A.; Yamaguchi, S., Analysis of Vinylene Carbonate Derived SEI Layers on Graphite Anode. *Journal of The Electrochemical Society* **2004,** *151* (10), A1659-A1669.
17. Dedryvère, R.; Martinez, H.; Leroy, S.; Lemordant, D.; Bonhomme, F.; Biensan, P.; Gonbeau, D., Surface film formation on electrodes in a LiCoO2/graphite cell: A step by step XPS study. *Journal of Power Sources* **2007,** *174* (2), 462-468.
18. Polovina, M.; Babić, B.; Kaluderović, B.; Dekanski, A., Surface characterization of oxidized activated carbon cloth. *Carbon* **1997,** *35* (8), 1047-1052.
19. Lesiak, B.; Jablonski, A.; Prussak, Z.; Mrozek, P., Experimental determination of the inelastic mean free path of electrons in solids. *Surface Science* **1989,** *223* (1), 213-232.
20. Tanuma, S.; Powell, C. J.; Penn, D. R., Calculations of electron inelastic mean free paths. IX. Data for 41 elemental solids over the 50 eV to 30 keV range. *Surface and Interface Analysis* **2011,** *43* (3), 689-713.
21. Tanuma, S.; Powell, C. J.; Penn, D. R., Calculations of electorn inelastic mean free paths. II. Data for 27 elements over the 50–2000 eV range. *Surface and Interface Analysis* **1991,** *17* (13), 911-926.
22. Biesinger, M. C., Advanced analysis of copper X-ray photoelectron spectra. *Surface and Interface Analysis* **2017,** *49* (13), 1325-1334.
23. Biesinger, M. C.; Payne, B. P.; Grosvenor, A. P.; Lau, L. W. M.; Gerson, A. R.; Smart, R. S. C., Resolving surface chemical states in XPS analysis of first row transition metals, oxides and hydroxides: Cr, Mn, Fe, Co and Ni. *Applied Surface Science* **2011,** *257* (7), 2717-2730.